Collaborative Control Framework of a Robotic Transesophageal Echocardiography System for Guiding Structural Heart Interventions

Xiu Zhang, Benjamín Ignacio Fortuño Jara, Matteo Di Mauro, Vanessa Cannizzaro, Angela Peloso, Anna Bicchi, *Student Member, IEEE,* Luca Vicentini, Andrea Aliverti, *Member, IEEE,* Emiliano Votta, Arianna Menciassi, *Fellow, IEEE*, and Elena De Momi, *Senior Member, IEEE* .

***Abstract*—Transesophageal Echocardiography (TEE) is important for guiding the surgeon in percutaneous intervention for structural heart diseases. TEE is acquired through a catheter-like probe that must be maneuvered by a sonographer. Also, since X-ray fluoroscopy is adopted along with TEE, surgeons and sonographers must wear heavy protective suits to shield against radiation, leading to fatigue and the long-term risk of musculoskeletal injuries. This work proposes a robotic TEE system with a collaborative control framework designed to autonomously adjust the TEE probe, while relieving sonographers from physical effort and X-ray exposure. To enable accurate task space control in the constrained anatomical environment, a hybrid adaptive controller is introduced, leveraging offline hysteresis data and real-time feedback from electromagnetic (EM) sensors. Experiments conducted on silicone-casted esophagus phantoms with varying thicknesses, as well as path following tests with different patterns, demonstrate the controller's adaptability and accuracy. The framework was further validated through a complete workflow simulation within a cardiac phantom, replicating a transcatheter mitral valve repair procedure. The system maintained a maximum angular error below 3.2°. The results highlight the potential of the proposed robotic system for clinical applications in robot-assisted intervention procedures.**

***Index Terms*—Medical robot and system, Adaptive control, Collaborative control, Transesophageal echocardiography.**

I. Introduction

Structural heart diseases are among the most common cardiac diseases worldwide, involving defects in the heart's muscles and valves that impact millions, particularly the elderly and patients at high surgical risk [1]. Minimally invasive percutaneous interventions, such as Left Atrial Appendage Occlusion (LAAO), and Transcatheter Mitral Valve repair (TMVr) and Replacement (TMVR), offer promising alternatives for patients who cannot undergo open-heart surgery, reducing trauma and hospitalization time [2]. In these procedures, such as TMVr, an implant (e.g., a clip) is delivered by the interventionalist using catheters through the blood vessels to grasp the mitral valve leaflets, thereby reducing mitral regurgitation. Pre-operatively, Computed Tomography (CT) plays a critical role in planning for these interventions, while fluoroscopy is employed intraoperatively to locate and position the catheters. Most importantly, interventionists rely on real-time imaging from the Transesophageal Echocardiography (TEE) probe, which is operated by a sonographer and provides high-resolution, multi-plane views of the heart chambers [3].

During these interventional procedures, the interventionalist communicates verbally with the sonographer, who must continuously manipulate the TEE probe to maintain the correct imaging configuration within the patient's esophagus [4]. Depending on the procedural phase, the sonographer may need to adjust the probe to visualize the catheter, focus on specific anatomical structures, or return to a previously acquired view. This process demands a high level of coordination within the surgical team [5]. Poor communication or insufficient collaboration among team members can prolong the intervention, thereby increasing the risk of complications of the TEE procedure [6]. Furthermore, the sonographist must work next to the surgical bed throughout the procedure, thus being exposed to radiation from the use of X-ray fluoroscopy [7].

In this work, we present an autonomous robotic TEE system that integrates an electromagnetic (EM) sensor to localize instruments inside the body. Building on our prior TEE robot [8], we introduce a closed-loop hybrid adaptive controller that combines offline hysteresis data with real-time EM feedback for accurate tip positioning. To the best of our knowledge, this is the first implementation of a catheter-following control strategy for a bendable ultrasound probe, allowing the robot to autonomously track the catheter tip and maintain it within the ultrasound field of view. The proposed system is validated in realistic in-vitro phantom experiments.

The main contributions of this paper are:

- A hybrid adaptive controller is developed to precisely position the TEE robot in the task space, effectively compensating for the inherent hysteresis effect and the constraints from the esophagus wall.

Xiu Zhang is with Department of Electronics, Information and Bioengineering, Politecnico di Milano, Milan 20133, Italy, and also with the BioRobotics Institute, Scuola Superiore Sant'Anna, 56025 Pontedera, Italy (Corresponding author: Xiu Zhang) (e-mail: xiu.zhang@santannapisa.it).

B.I. Fortuño, M. Di Mauro, C. Vanessa, A. Peloso, A. Bicchi, A. Aliverti, E. Votta, E. De Momi are with the Department of Electronics, Information and Bioengineering, Politecnico di Milano, Milan 20133, Italy (e-mail: benjaminignacio.fortuno, matteo. dimauro, vanessa.cannizzaro, angela.peloso, anna.bicchi, andrea.aliverti, emiliano.votta, elena.demomi)@polimi.it

Luca Vicentini is with SIMULANDS, GmbH, Switzland (email: luca@simulands.com)

Arianna Menciassi is with the BioRobotics Institute, Scuola Superiore Sant'Anna, 56025 Pontedera, Italy (e-mail: arianna.menciassi@santannapisa.it).

This work was supported by the European Union's Horizon 2020 research and innovation program under the ARTERY grant agreement No. 101017140.

- A catheter-following control algorithm is proposed to allow the TEE robot to autonomously adjust its pose to track the catheter, which allows visualization of the catheter tip always in the echo image.
- The proposed methods are implemented on a robotic TEE system and validated in an in vitro setup, with a visual interface that registers instrument-localized information to preoperative anatomical data.

The rest of this article is organized as follows. We first introduce the related work in Section II. The details of the proposed robotic TEE system and the collaborative control framework are described in Section III. Section IV presents our validation method and experimental results, and finally, Section V provides the conclusions of this study.

II. Related work

In recent years, Robotic UltraSound Systems (RUSS) have emerged as a rapidly evolving field, demonstrating significant potential to automate ultrasound acquisitions with enhanced accuracy and reproducibility [9]–[11]. Among them, the TEE probe, which consists of an ultrasound transducer mounted at a tendon-actuated bendable tip and a flexible insertion shaft, enables high-quality imaging of the cardiac chambers through the esophagus. Wang et al. developed one of the first robotic TEE systems to automate ultrasound acquisition and reduce operator dependency [12], [13]. While the system achieved repeatable positioning in phantom experiments, its control framework was limited to the actuation space and lacked task-level autonomy.

The integration of EM sensors on surgical tools and registration within images during cardiac interventions provides the benefit of real-time catheter localization without relying on fluoroscopy [14]–[16]. This advancement also enables closed-loop control by allowing direct measurement of the catheter tip position. Model-based control approaches, particularly those employing constant curvature (CC) theory, are widely adopted in the control of tendon-driven continuum robots due to their simplicity and computational efficiency [17]–[19]. To improve model accuracy, more advanced kinematic formulations have been proposed. For example, Ahmad et al. proposed a robust control framework based on Cosserat rod theory to better capture elastic deformation and bending behavior [20]. However, such models often fail to fully account for system nonlinearities and experience degraded performance in the presence of strong hysteresis effects.

To address these limitations, fuzzy logic theory has been introduced to improve the controller performance by compensating hysteresis effect in tendon-driven mechanisms [21], [22]. Ba et al. employed a Piecewise Constant Curvature (PCC) model to develop a fuzzy-logic controller to improve control precision [23]. Nevertheless, these methods typically require extensive manual tuning of fuzzy rules and parameters. Consequently, improving closed-loop control performance in the presence of hysteresis remains an important challenge, especially in practical implementations where conventional linear controllers are commonly used as baseline solutions.

Building on accurate position control in task space, collaborative control strategies have been introduced to intuitively provide real-time images of surgical instruments. One notable example is the work by Omid et al., who developed an autonomous robotic transrectal ultrasound system designed to track da Vinci instruments during laparoscopic radical prostatectomy [24]. Paul et al. proposed an image spinning strategy for automatically positioning an intracardiac ultrasound catheter to track the target [25]. However, these methods typically rely on manually placing the ultrasound probe in a proper position and then rotating it around its axial axis to bring the target into the ultrasound scan plane. Moreover, the automation and collaborative control of TEE probe manipulation, as well as its integration into structural heart intervention workflows for catheter guidance in constrained anatomical environments, remain insufficiently addressed.

III. Materials and Methods

A. Robotic TEE System

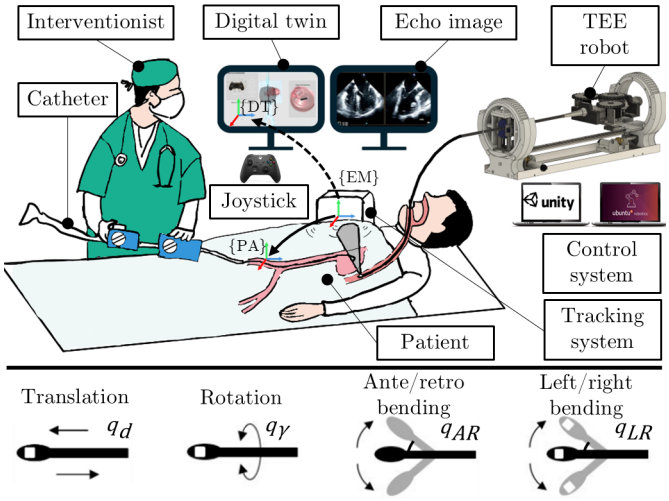

Fig. 1. Robotic TEE system: In the operating room, the TEE robot secures the TEE probe after insertion into the esophagus, enabling precise control across all 4-DoFs. Following registration, the catheter, TEE probe, visual interface, and patient anatomy are aligned within the EM reference frame EM. The interventionist navigates the catheter inside the heart using visual feedback from the echo image provided by the TEE and the visual interface, which integrates EM sensor data with preoperative CT images. Additionally, the interventionist can interact with the robotic system via a joystick for direct control and adjustments.

The proposed robotic TEE system enables the interventionist to perform the catheter navigation within the heart while the TEE robot operates alongside the patient (Fig. 1). The system is composed of three key components:

- TEE Robot: The robot actuates all the 4-DOFs of the TEE probe automatically, including: translating and rotating along the axis direction by moving the TEE probe from the proximal handle; and bending in two directions, e.g. ante/retro (AR) and left/right (LR) directions through the tendon-driven mechanism.
- Tracking system: This system provides real-time pose information for both the catheter and the TEE probe in the EM reference frame {EM}. By following a point to point registration procedure developed in prior work [26], the EM reference frame {EM} can be registered with

the patient reference frame, {PA}, which is also aligned with the visual interface reference frame {DT}, as they represent the same anatomical structure [27].

- Intraoperative visual feedback: Two monitors display relevant information to the interventionist. One displays the echo images captured by the TEE probe, while the other presents a virtual visual interface consisting of the patient's anatomy reconstructed from pre-operative CT scans, where the virtual avatars of the TEE probe and of the catheter are visualized based on sensor data and geometrical modeling.

B. TEE Robot Kinematics

The TEE robot actuates the TEE probe in the joint space, $\boldsymbol{q} \in \mathbb{R}^4$, defined by four actuator variables: ante/retro bending (q_{AR}), left/right bending (q_{LR}), rotation (q_γ), and translation (q_d) [8]. On the other hand, the TEE probe is an underactuated system whose task space is characterized by the pose vector, $\boldsymbol{\xi}_{tip} = [\boldsymbol{p}_{tip}, \gamma]^T \in \mathbb{R}^4$, where $\boldsymbol{p}_{tip}$ represents the position of the probe tip and γ is the roll angle. To enable the collaborative control framework, it is essential to compute the inverse kinematics, which maps the desired task-space pose to the corresponding joint-space actuation variables.

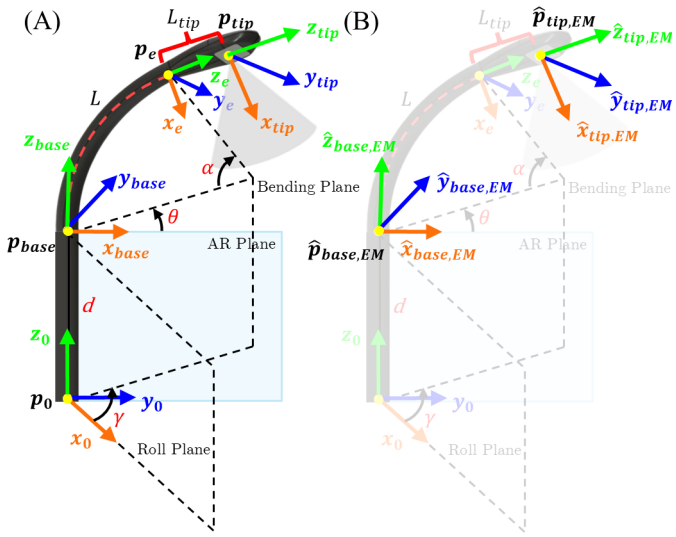

Fig. 2. Kinematics of the TEE probe: (A) Forward kinematics of the TEE probe include: translation (d), roll angle (γ), rotation angle between the AR plane and the bending plane (θ), bending angle (α), length of the bending section (L) and length of the tip (L_{tip}). (B) The pose measurements are acquired using EM sensors at both the tip and the base of the TEE probe.

The TEE robot works as a TDCR, which can be modeled using a CC model. As shown in Fig. 2A, frame 0 is defined as the origin of the robot. The base of the TEE probe is obtained by rotating along the z-axis by the roll angle (γ). Under the constant curvature assumption, the configuration of the bending section is defined by the rotation angle (θ), the bending angle (α), and the length of the bending section (L). The tip pose of the TEE probe is then derived by applying a rigid translation from the end-effector pose $[\boldsymbol{p}_e, \boldsymbol{x}_e, \boldsymbol{y}_e, \boldsymbol{z}_e]^T$ along the $\boldsymbol{z}_e$ direction by a distance L_{tip}. The forward kinematics is represented by the transformation matrix $\mathbf{T}(d, \gamma, \theta, \alpha, L, L_{tip})$.

The inverse kinematics can be solved accordingly following the method proposed by Degirmenci et al. [19].

Among the joint-space variables, the translation (d) and probe base roll (γ) are directly controlled by the translation (q_d) and the roll (q_γ) commands in the joint space independently. While the ante/retro bending (q_{AR}), left/right bending (q_{LR}) can be calculated using θ and α based on following equations:

$$\begin{aligned} q_{AR} &= \arcsin\left(|\sin\alpha \sin\theta|\right) \\ q_{LR} &= \arcsin\left(|\sin\alpha \cos\theta|\right) \end{aligned} \tag{1}$$

Additionally, EM sensors measure poses of both the tip and the base of the TEE probe in Cartesian coordinates, yielding $\hat{\boldsymbol{\xi}}_{tip,EM} = [\hat{\boldsymbol{p}}_{tip,EM}, \hat{\boldsymbol{x}}_{tip,EM}, \hat{\boldsymbol{y}}_{tip,EM}, \hat{\boldsymbol{z}}_{tip,EM}]^T$, $\hat{\boldsymbol{\xi}}_{base,EM} = [\hat{\boldsymbol{p}}_{base,EM}, \hat{\boldsymbol{x}}_{base,EM}, \hat{\boldsymbol{y}}_{base,EM}, \hat{\boldsymbol{z}}_{base,EM}]^T \in \mathbb{R}^6$. These measurements are subsequently converted to the joint space through the inverse kinematics procedure (Fig. 2B).

C. Clinical workflow

The proposed control framework for guiding structural heart interventions follows a four-step workflow (Supplementary Video 3):

- Step 1: Calibration
  A calibration is performed between the EM reference frame {EM} and the patient visual interface {DT} reference frame using corresponding 3D printed points [26].
- Step 2: Anatomical landmark identification
  The operator manually inserts the TEE probe into the esophagus and uses the joystick to teleoperate the TEE robot to locate the anatomical landmark. Once the landmark is clearly visualized, the pose of the TEE probe is saved as the stored pose ($\boldsymbol{\xi}^s_{tip}$) for post-operative evaluation (Step 4).
- Step 3: Delivery of the implant
  After the catheter accesses the heart chamber with the implant, the TEE robot is switched to "catheter following mode". During this stage, the operator manually maneuvers the catheter to position the implant at the identified landmark. Simultaneously, the TEE robot autonomously follows the catheter, providing continuous real-time visual feedback to support precise implant delivery.
- Step 4: Post-operative evaluation
  Once the implant has been delivered, the TEE robot operates in "location retract mode". It autonomously returns to the stored pose ($\boldsymbol{\xi}^s_{tip}$) by a sequence of movement, minimizing the risk of esophageal wall damage caused by large bending angles.

D. Collaborative Control Framework

The collaborative control framework integrates a hybrid adaptive controller with two distinct target-defined modes to achieve precise TEE robot control (Fig. 3). The hybrid adaptive controller receives the desired tip pose ($\boldsymbol{\xi}_{tip}$) as input and combines real-time feedback from the measured tip ($\hat{\boldsymbol{\xi}}_{tip,EM}$) and base ($\hat{\boldsymbol{\xi}}_{base,EM}$) pose of the TEE probe to autonomously adjust the robot.

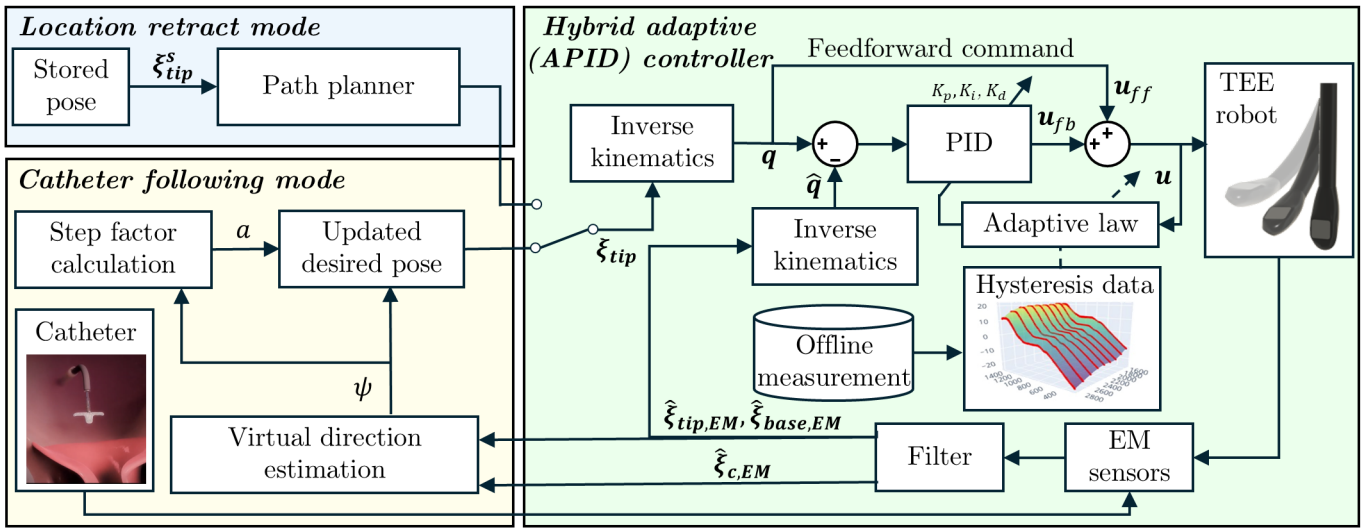

Fig. 3. Collaborative control framework includes two modes of operation. The location retract mode automatically adjusts the TEE probe to a predefined position to visualize the anatomical target, while the catheter following mode dynamically adjusts the TEE probe to follow the catheter. Both modes generate the desired pose ($\boldsymbol{\xi}_{tip}$) as input for the hybrid adaptive controller, which ensures pose control of the TEE robot through a feedforward-feedback control loop.

1) Catheter Following Mode: This strategy involves determining a movement direction that points the current positive x-axis of the TEE tip measured by the EM sensor ($\hat{\boldsymbol{x}}_{tip,EM}$) with the measured catheter position ($\hat{\boldsymbol{p}}_{c,EM}$). This alignment ensures that the ultrasound crystal located at the TEE tip, which generates a linear ultrasound beam in the normal direction, points directly at the desired target.

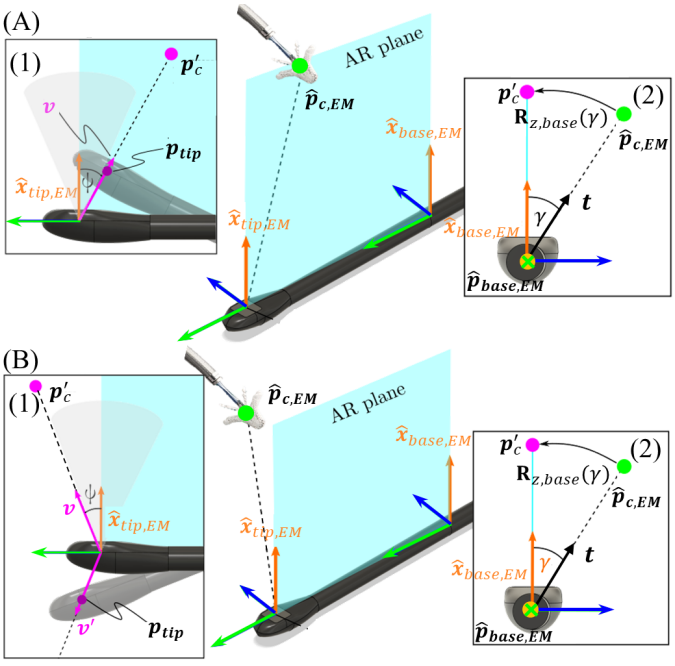

Fig. 4. Two cases in catheter following mode: (A) The target point lies behind the TEE probe, characterized by a negative z-component relative to the tip. In this case, the vector $\boldsymbol{v}$ is applied directly to align the probe with ante bending. (B) The target point is in front of the TEE probe, characterized by a positive z-component relative to the tip. Here, the vector $\boldsymbol{v}$ is replaced with its mirrored vector $\boldsymbol{v}'$ to adjust the probe with retro bending.

By maintaining this alignment, the target remains centered in the echo image. The algorithm iteratively adjusts the pose using ante-bending or retro-bending (Fig. 4). The process begins by extracting the position components from the measured TEE base pose ($\hat{\boldsymbol{\xi}}_{base,EM}$) and the catheter pose ($\hat{\boldsymbol{\xi}}_{c,EM}$), denoted as $\hat{\boldsymbol{p}}_{base,EM}$ and $\hat{\boldsymbol{p}}_{c,EM}$, respectively. Then the vector $\boldsymbol{t}$ is calculated, which represents the direction from $\hat{\boldsymbol{p}}_{base,EM}$ to $\hat{\boldsymbol{p}}_{c,EM}$. As shown in Fig. 4 (A2), the roll angle γ along the z-axis is computed between the vector $\boldsymbol{t}$ and positive x-axis of the base pose ($\hat{\boldsymbol{x}}_{base,EM}$) to align the target inside the AR plane. Then, an auxiliary point $\boldsymbol{p}'_c$ is identified by rotating the measured catheter position $\hat{\boldsymbol{p}}_{c,EM}$ along the z-axis with the roll angle γ into the AR bending plane. This rotation is expressed as:

$$\boldsymbol{p}'_c = \mathbf{R}_{z,base}(\gamma)\hat{\boldsymbol{p}}_{c,EM} \tag{2}$$

Here, $\mathbf{R}_{z,base}(\gamma)$ represents a rotation along the z-axis of the base with an angle, γ.

Although this rotation aligns the catheter within the AR plane, the target may still not be visible in the fan-shaped echo image unless the TEE probe is correctly oriented. To address this, the vector $\boldsymbol{v}$, pointing from the current TEE tip position ($\hat{\boldsymbol{p}}_{tip,EM}$) to the auxiliary point ($\boldsymbol{p}'_c$), is calculated, representing the pointing direction. The deviation angle ψ is derived between the vector $\boldsymbol{v}$ and the orientation vector of the TEE tip ($\hat{\mathbf{x}}_{tip,EM}$) as follows:

$$\psi = \cos^{-1}\left(\frac{\boldsymbol{v} \cdot \hat{\boldsymbol{x}}_{tip,EM}}{||\boldsymbol{v}|| \cdot ||\hat{\boldsymbol{x}}_{tip,EM}||}\right) \tag{3}$$

If $\psi > 0$, as shown in Fig. 4 (A1), the target is located superior to the TEE probe's orientation. In this scenario, the TEE probe bends in the anterior direction to align itself with the target. Conversely, if $\psi < 0$, as shown in case Fig. 4 (B1), the target is located inferior to the TEE probe's orientation. In this case, the vector $\boldsymbol{v}$ is interpreted as pointing to the opposite side of the TEE probe. Conceptually, this formulation flips the direction to guide the probe in the retroflexion direction along a new vector $\boldsymbol{v}'$, enabling proper alignment with the target.

To ensure smooth convergence toward the target, the step length in the search process is governed by a step factor a. This factor dynamically adjusts based on the magnitude of ψ. using a sigmoid function with the sensitivity parameter α and ψ_0:

$$a = \frac{2}{1 + e^{-\alpha(\psi - \psi_0)}} \tag{4}$$

The sigmoid function ensures a gradual transition, allowing larger steps when the deviation is significant and smaller steps as the alignment improves.

Finally, the desired position ($\boldsymbol{p}_{tip}$) is iteratively updated by applying the scaled vector $\boldsymbol{v}$ to the current tip position $\hat{\boldsymbol{x}}_{tip,EM}$. The update continues until the deviation angle ψ falls below a predefined threshold, 2°, which was chosen as a practical compromise to ensure accurate alignment while avoiding excessive control effort and unstable echo image.

$$\boldsymbol{p}_{tip}[k+1] = \hat{\boldsymbol{x}}_{tip,EM}[k] + a \cdot \boldsymbol{v} \tag{5}$$

This iterative approach, shown in Algorithm 1, ensures that the TEE probe incrementally aligns with the target, minimizing overshoot and enabling precise orientation for optimal visualization of the target within the echo image.

Algorithm 1 Catheter Following Mode

Input: $\hat{\boldsymbol{p}}_{c,EM}, \hat{\boldsymbol{p}}_{base,EM}, \hat{\boldsymbol{p}}_{tip,EM}, \hat{\boldsymbol{x}}_{base,EM}, \alpha, \psi_0$
Output: $\boldsymbol{p}_{tip}[k+1]$
// Calculate the vector $\boldsymbol{t}$
$\boldsymbol{t} = \hat{\boldsymbol{p}}_{c,EM} - \hat{\boldsymbol{p}}_{base,EM}$
// Determine the roll angle γ
$\gamma = \text{atan2}(\|\boldsymbol{t} \times \hat{\boldsymbol{x}}_{base,EM}\|, \boldsymbol{t} \cdot \hat{\boldsymbol{x}}_{base,EM})$
// Identify the auxiliary point
$\boldsymbol{p}'_c = \mathbf{R}_{z,base}(\gamma)\hat{\boldsymbol{p}}_{c,EM}$
$\boldsymbol{v} = \hat{\boldsymbol{p}}_{tip,EM} - \boldsymbol{p}'_c$
// Compute the deviation angle ψ
$\psi = \cos^{-1}\left(\frac{\boldsymbol{v} \cdot \hat{\boldsymbol{x}}_{tip,EM}}{\|\boldsymbol{v}\| \cdot \|\hat{\boldsymbol{x}}_{tip,EM}\|}\right)$
if $\psi < 0$ **then**
    // Case A: target behind probe (negative z-component) $\boldsymbol{v}$ is applied directly
else
    //Case B: target in front (positive z-component) $\boldsymbol{v}' = R_{z,\text{tip}}(180°)\boldsymbol{v}$ is applied
end if
// Determine the step factor a
$a = \frac{2}{1+e^{-\alpha(\psi-\psi_0)}}$
// Update the desired position
$\boldsymbol{p}_{tip}[k+1] = \hat{\boldsymbol{x}}_{tip,EM}[k] + a \cdot \boldsymbol{v}$

2) Location Retract Mode: The location retract mode employs a path planning strategy to safely guide the TEE probe back to the stored pose ($\boldsymbol{\xi}^s_{tip}$) within the esophagus (Fig. 5). This mode ensures controlled and safe manipulation of the probe in a confined anatomical space. The sequence of movements can be described as follows:

1) Initial Positioning: The probe moves from its current pose (ξ_{tip}) to align with the centerline of the esophagus. To minimize potential risks, the ante/retro bending (q_{AR}) and left/right bending (q_{LR}) are released, reducing large bending angles that could harm the esophageal wall during rotation and translation.
2) Alignment: The probe rotates (q_γ) along the axial direction to match its orientation with the target angle (Fig. 5). Following this, the probe advances (q_d) along the esophageal centerline to reach the midpoint ($\boldsymbol{p}^s_{tip}{}'$), which is projected as an intermediate point on the path toward the target pose.
3) Movement to Target point: Starting from the $\boldsymbol{p}^s_{tip}{}'$, the probe is actuated within the axial plane, incorporating precise bending motions to navigate toward and reach the stored pose ($\boldsymbol{\xi}^s_{tip}$). The path is defined by linearly interpolating between the midpoint and the target.

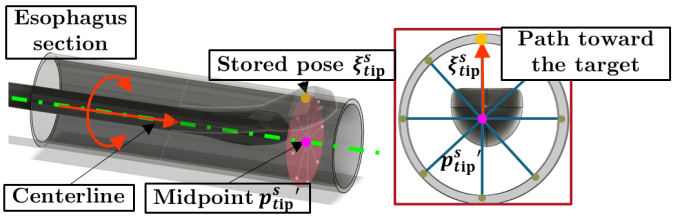

Fig. 5. Location retract mode: Left panel illustrates the path planning within the esophagus, guiding the TEE probe back to the stored pose. Right panel shows the resulting path visualized in the axial plane.

3) Hybrid Adaptive Controller: The hybrid adaptive (APID) controller computes the actuation commands, $\boldsymbol{u} \in \mathbb{R}^4$, by combining the feedforward command, $\boldsymbol{u}_{ff}$ and the feedback command, $\boldsymbol{u}_{fb}$. The current tip pose ($\hat{\boldsymbol{\xi}}_{tip,EM}$) and base pose ($\hat{\boldsymbol{\xi}}_{base,EM}$) are measured from two EM sensors attached at the tip and base of the bending section. The EM sensors operated at a sampling frequency of 40 Hz, and the acquired data were smoothed using a median filter applied over every 10 consecutive samples to mitigate high-frequency noise and transient outliers. This filtering strategy is consistent with prior studies reporting EM tracking distortions caused by nearby metallic objects and magnetic field interference [28], [29]. With the inverse kinematics described earlier, both the measured pose ($\hat{\boldsymbol{\xi}}_{tip,EM}, \hat{\boldsymbol{\xi}}_{base,EM}$) and desired pose ($\boldsymbol{\xi}_{tip}$) in the task space are converted into joint space variables $\hat{\boldsymbol{q}}$ and $\boldsymbol{q}$. The desired joint-space variables $\boldsymbol{q}$ serves as the feedforward command, $\boldsymbol{u}_{ff}$.

The error between $\hat{\boldsymbol{q}}$ and $\boldsymbol{q}$ is processed by the PID controller to compute the feedback command, $\boldsymbol{u}_{fb}$. In the feedback control loop, the proportional, integral, and derivative constants (K_p, K_i, K_d) are organized into a diagonal matrix $\in \mathbb{R}^{4x4}$. Due to the significant hysteresis effects introduced by the tendon-driven mechanism actuating the AR and the LR bending, the bending parameters for AR and LR movements are adapted dynamically based on a data-driven hysteresis model. In contrast, the constants for translation and rotation remain fixed.

In [8], the hysteresis behavior was modeled with free-knot B-spline curves for positive and negative directions independently. To account for the coupling between AR and LR bending, we extend the model to a bivariate B-spline surface

(f and g), which relates actuation inputs (u_{AR}, u_{LR}) to the bending angles (q_{AR}, q_{LR}) as follows:

$$\begin{aligned} q_{AR} &= f(u_{AR}, u_{LR}) \\ q_{LR} &= g(u_{AR}, u_{LR}) \end{aligned} \tag{6}$$

To construct these hysteresis models, an offline dataset is collected by systematically actuating the robotic TEE probe. The probe is sequentially bent in AR and LR directions—first by fixing the AR bending angle while varying LR to span its full range, then incrementally adjusting AR with repeated LR sweeps, and finally reversing the process to achieve complete workspace coverage. The dataset comprises 39,600 samples of measured tip and base poses ($\hat{\xi}_{tip,EM,i}$· $\hat{\xi}_{base,EM,i}$), which are converted to bending angles ($\hat{q}_{AR,i}, \hat{q}_{LR,i}$) using inverse kinematics. These data, along with their corresponding actuation inputs ($u_{AR,i}$, $u_{LR,i}$). are used to optimize a bivariate spline representation of hysteresis. Using the deterministic optimization approach proposed by Beliakov et al. [30], a bivariate spline fitting is performed via the Gauss-Newton method to identify the underlying hysteresis model. Notably, dead zones in the hysteresis response are observed in the middle part of the dataset (Fig. 3).

The APID coefficients are dynamically adjusted based on the identified hysteresis models. The derivatives, $\delta_1 = \frac{\partial f}{\partial u_{AR}}$ and $\delta_2 = \frac{\partial g}{\partial u_{LR}}$, are computed to capture the rate of change in bending angles. The adaptive law updates APID coefficients using the following functions, ensuring smooth transitions without abrupt changes:

$$K_p = \begin{cases} K_{p0}\left(1 + \alpha\left(1 - \frac{|\delta_j|}{\epsilon}\right)\right) & \text{if } |\delta_j| < \epsilon, \\ K_{p0} & \text{if } |\delta_j| \geq \epsilon, \end{cases} \tag{7}$$

$$K_i = \begin{cases} K_{i0}\left(1 + \beta\left(1 - \frac{|\delta_j|}{\epsilon}\right)\right) & \text{if } |\delta_j| < \epsilon, \\ K_{i0} & \text{if } |\delta_j| \geq \epsilon, \end{cases} \tag{8}$$

$$K_d = \begin{cases} K_{d0}\left(1 - \gamma\left(1 - \frac{|\delta_j|}{\epsilon}\right)\right) & \text{if } |\delta_j| < \epsilon, \\ K_{d0} & \text{if } |\delta_j| \geq \epsilon. \end{cases} \tag{9}$$

Here, α, β, and γ are positive scaling factors that determine the extent of gain adjustment. If the derivative magnitude, $|\delta_j|$ exceeds the threshold ϵ, the gains are maintained at their baseline values (K_{p0}, K_{i0}, and K_{d0}) to ensure system stability. Conversely, when $|\delta_j|$ falls into the threshold ($|\delta_j| < \epsilon$), indicates that the system is operating in a dead zone. Based on the offline hysteresis data, this dead zone can be clearly identified in the middle of the bending range, where sudden changes occur in the derivative of the response curves. The threshold ϵ is therefore defined as the maximum derivative within the dead zone area across all datasets. Within this region, the adaptive gains enhance performance by making the system more responsive (higher K_p and K_i), and less sensitive to noise (lower K_d), depending on the deviation magnitude.

IV. Experiments and Results

A. Experimental setup

The proposed control framework was evaluated using the system depicted in Fig. 6. A TEE probe (X7-2t, Philips, Netherlands) was mounted on a robotic actuation system. The translation (q_d) was driven by a friction roller system coupled with a DC-gear motor (Faulhaber Series 2619S006SR 361 : 1, Germany), and roll (q_γ) was actuated via two gear wheels powered by a Faulhaber motor (Series 2250S024BX4 SC, Germany). While the AR bending (q_{AR}) and LR bending (q_{LR}) were separately controlled through a spur gear mechanism and a DC servomotor (Dynamixel XM350-T, South Korea) [8].

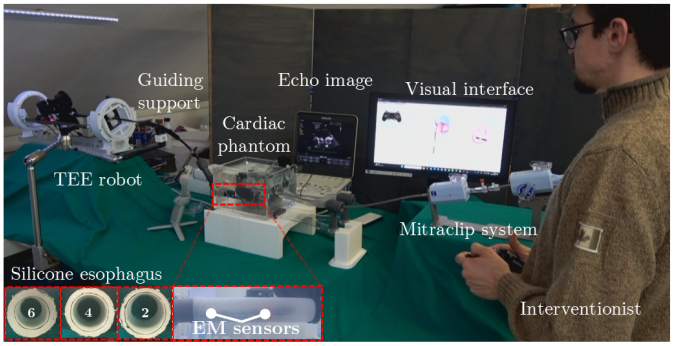

Fig. 6. Experimental setup: The TEE robot manipulates the probe in the cardiac phantom, which features a silicone esophagus model with three different thicknesses of 6, 4, 2 mm. EM sensors are attached to both the MitraClip and the TEE to provide real-time pose tracking. The operator can either manually control the TEE robot via a joystick or steer the MitraClip system, while the TEE robot autonomously follows the catheter tip. Visual feedback is provided through the echo image system and a visual interface.

For the catheter intervention task, a transcatheter system (MitraClip, Abbott, US) was employed to simulate an edge-to-edge mitral valve repair procedure. The experimental setup was integrated with a cardiac phantom (Slice Simulator, SIMULANDS, Switzerland) featuring a detachable silicone esophagus. The TEE probe was inserted through a passive guiding support into the esophagus, while the catheter was introduced from the simulated femoral vein access.

The EM tracking system (Aurora, NDI, Canada) provided real-time pose measurements of the TEE probe at a frequency of 40 Hz using two 6-DOF EM sensors attached to the probe with a position error of 1.4 mm and orientation error of 3.6°. The two EM sensors were mounted at the tip and base of the probe to capture its spatial configuration during motion. A key challenge was aligning the EM tracker frame with the probe's sagittal plane. To address this, the probe performed an AR bending motion with a fixed base, and the relative displacement between the two sensors was used to estimate the actual bending plane. The resulting deviation angle was computed and compensated to correct torsional misalignment, ensuring accurate correspondence between the EM-measured and physical probe motion.

A visual interface was developed in Unity (Unity Technologies, USA) to provide real-time visual feedback during the robotic TEE procedure (Supplementary Video 3). The central display presents a 3D model of the phantom with the TEE probe and catheter, both reconstructed from EM data and registered to the physical setup through a point-to-point calibration using six fiducial pillars placed alongside the phantom [26]. The interface includes interactive buttons that allow toggling the visibility of the phantom, heart, and TEE

probe, as well as control instructions for the connected joystick (PS2, SONY, Japan) to guide operator input. Additionally, a zoomed-in view of the mitral valve is displayed to assist in precise implant alignment.

For statistical analysis, results from each group were first examined for normality using the Shapiro–Wilk test. Since the normality assumption was violated for all groups, nonparametric Kruskal–Wallis tests were used to evaluate statistically significant differences among algorithms.

B. Path following experiment

The experiments were designed to evaluate the accuracy and adaptability of the proposed controller under various path patterns and velocities. Each test was repeated three times. The position error ($e_{p,i}$), defined as the norm of the difference between the desired position on the path ($\boldsymbol{p}_{tip,i}$) and the current position ($\hat{\boldsymbol{p}}_{tip,EM,i}$), measured by the EM sensor:

$$e_{p,i} = \|\boldsymbol{p}_{tip,i} - \hat{\boldsymbol{p}}_{tip,EM,i}\| \tag{10}$$

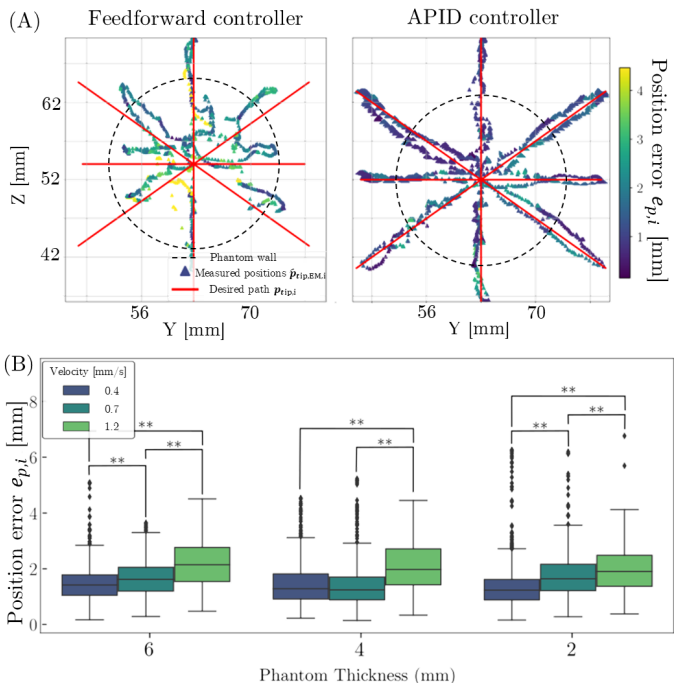

Fig. 7. Results in the constrained environment: (A) The feedforward controller fails to accurately follow the desired path, especially at the extremities, resulting in significant position errors, whereas the APID controller demonstrates improved performance; (B) Distributions of the position error in a constrained environment experiment. The boxplot illustrates the position error of the APID controller among different phantom thicknesses (2, 4, and 6 mm) and velocities (0.4, 0.7, and 1.2 mm/s). ** : p-value < 0.005.

1) Evaluation in Constrained Environment: In the clinical scenario, the TEE probe is inserted and manipulated inside the esophagus, where the constrained environment introduces challenges to the proposed position controller. Clinical studies indicate that the retrocardiac portion of the human esophagus has an average wall thickness of 2 mm with a modulus of elasticity of 0.86 MPa [31], [32]. To consider intersubject anatomical variability, esophagus phantoms were designed as cylindrical tubes with an inner diameter of 20 mm and thicknesses of 6, 4, 2 mm (Fig. 6). These phantoms were cast using silicone (Dragon skin FX-Pro, Smooth-on, US), with a 100% modulus (M_{100}) of 0.26 MPa.

A star-shaped path was defined to evaluate the "location retract mode" ensuring safe and precise movement near the esophagus wall. A feedforward controller, which computes actuation commands using the inverse kinematics of the TEE, was used as a baseline for comparison with the proposed hybrid adaptive (APID) controller. The experimental comparison was carried out in a 2 mm thick silicone esophagus at a velocity of 0.4 mm/s.

Fig. 7A shows the limitations of the feedforward controller, which fails to follow the desired path accurately, particularly at positions far from the center where the probe tip contacts the phantom wall. In general, the feedforward controller exhibited a median position error of 3.75 mm with an interquartile range (IQR) of 1.23 mm. In contrast, the APID controller dynamically adjusted the control inputs through real-time feedback, reducing the median position error to 2.07 mm with an IQR of 1.03 mm.

The APID controller was further evaluated using three silicone esophagus phantoms with wall thicknesses of 6, 4, 2 mm, and at three different velocities 0.4, 0.7, and 1.2 mm/s. The Kruskal-Wallis test was conducted to statistically analyze the differences among these tests. Fig. 7B presents the results of the proposed APID controller across all tests, showing that the median position error remained below 2.2 mm in all cases. Position errors were observed to increase with higher velocity. Moreover, it is noteworthy that the position errors did not exhibit significant differences across phantoms of varying thicknesses when assessed at the same velocity, suggesting that the proposed controller effectively adapts to phantoms of varying thickness, representing different anatomical conditions. This adaptability underscores the robustness of the APID controller in diverse constrained environments.

2) Evaluation with different path patterns: This experiment was conducted to evaluate the performance of the proposed APID controller in comparison with a conventional PID controller and a Fuzzy PID (FPID) controller, as a benchmark [33]. The focus was on assessing control accuracy, particularly in the dead zone of the bending movements (e.g., when the motors for AR and LR rotate but the TEE tip does not respond as expected). Three distinct geometric paths, a square, a circle, and a triangle, as shown in Fig. 8(A-C). Since the APID controller perforemed good at the constrained environment, this test were tested at three velocities 0.5, 1.0, and 1.5 mm/s, which is heigher to push the limit of the porposed controller. The Kruskal–Wallis test was employed to statistically analyze differences among the various test conditions.

The PID controller was tuned using the Ziegler-Nichols method, resulting in optimal gains of $K_p = 0.65$, $K_i = 0.0075$, and $K_d = 0.002$. For the FPID controller, Gaussian membership functions were employed, and fuzzy rules were defined to dynamically adjust the gains (K_p, K_i, and K_d) based on the position error (e_p) and the rate of change in error ($\frac{\partial e_p}{\partial t}$). The fuzzy rule table used to define these adjustments is shown in Table I.

TABLE I
FUZZY RULES FOR CONTROL GAINS

Input		Output		
e_p	$\frac{\partial e_p}{\partial t}$	K_p	K_i	K_d
Negative	Negative	Increase	Decrease	Increase
Negative	Zero	Maintain	Maintain	Increase
Negative	Positive	Decrease	Increase	Decrease
Zero	Negative	Increase	Decrease	Increase
Zero	Zero	Maintain	Maintain	Maintain
Zero	Positive	Decrease	Increase	Decrease
Positive	Negative	Increase	Decrease	Increase
Positive	Zero	Maintain	Maintain	Increase
Positive	Positive	Decrease	Increase	Decrease

Fig. 8D-F illustrates the results for three different paths. The APID controller consistently demonstrates superior performance and maintains a median position error below 2 mm across all paths and velocities. In contrast, the conventional PID controller exhibited significantly higher position errors, particularly for the square path where a large deviation is observed at the lower-right corner (Fig. 8A).

To evaluate the controller's performance in compensating for the dead zone, two metrics were introduced: the dead zone ratio (DZ_{ratio}) and dead zone rejection ratio (DZRR). DZ_{ratio} quantifies the controller's performance within the dead zone relative to that outside it, as defined by:

$$\mathrm{DZ}_{ratio} = \frac{median(e_{in,i})}{median(e_{out,i})} \tag{11}$$

Subsequently, using the conventional PID controller as the baseline, the DZRR is defined as:

$$\mathrm{DZRR} = \frac{\mathrm{DZ}_{ratio,\mathrm{controller}} - \mathrm{DZ}_{ratio,\mathrm{PID}}}{\mathrm{DZ}_{ratio,\mathrm{PID}}} \tag{12}$$

The dead zone area of the TEE probe was identified using the offline dataset described in Section III-D3. The position error ($e_{p,i}$) was computed with Equation 10 and categorized into two groups: $e_{in,i}$ representing position errors within the dead zone ($|\delta_j| < \epsilon$), and $e_{out,i}$, representing errors outside the dead zone ($|\delta_j| \geq \epsilon$).

Table II summarizes the median and IQR of position errors both inside and outside the dead zone, along with the DZRR values for the different control strategies at various velocities. In general, position errors increased with higher velocities; however, the APID controller consistently maintained the smallest median errors both within and outside the dead zone compared with the PID and FPID controllers. The PID controller exhibited higher position errors within the dead zone than outside of it, underscoring the significant impact of hysteresis on its performance. The FPID and APID controllers showed similar performance at non-slow velocities (1.0 and 1.5 mm/s), with both achieving DZRR values around 50%, indicating effective rejection of hysteresis. At the lower velocity of 0.5 mm/s, however, their performance diverged: the proposed APID controller achieved a DZRR of 18.12%, compared with only 0.60% for FPID. The low DZRR values at this speed suggest that hysteresis is less significant under slow motion, but the results also demonstrate that the APID controller adapts more effectively to the hysteresis characteristics by autonomously tuning PID gains based on offline data.

C. Catheter following experiment

In the experiment, the operator (a clinical specialist with three years of experience supporting interventional procedures) was tasked with navigating the catheter from the septal entry point toward the mitral valve. Following standard procedural

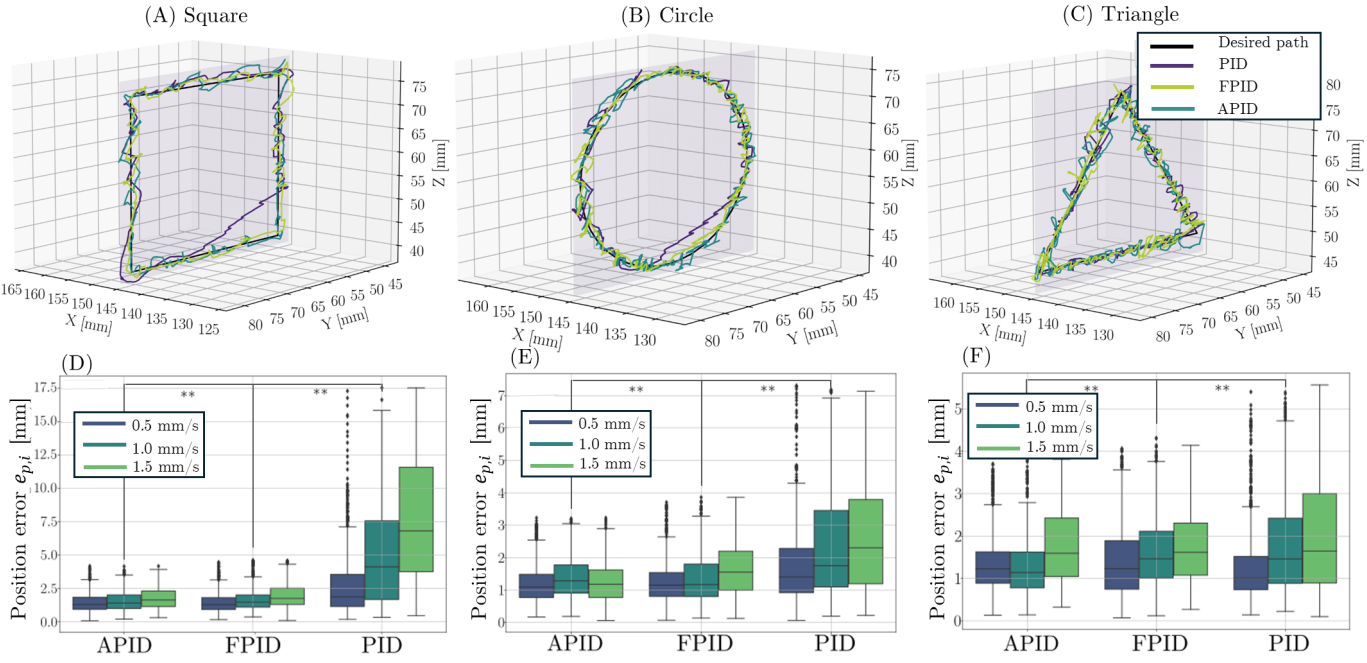

Fig. 8. Comparison of the APID controller with the conventional PID and FPID controllers across three different path patterns: (A-C) Three path patterns used for evaluation: square, circle and triangle. (D-F) Boxplots of the position errors for each controller at various velocities. ** : p-value < 0.005.

TABLE II
MEDIAN AND IQR OF POSITION ERROR (MM) INSIDE AND OUTSIDE THE DEAD ZONE, AND DEAD ZONE REDUCTION RATIO (DZRR) FOR DIFFERENT CONTROL STRATEGIES AND VELOCITIES IN THE SQUARE PATH.

Velocity (mm/s)	PID			FPID			APID		
	in DZ	out DZ	DZRR (%)	in DZ	out DZ	DZRR (%)	in DZ	out DZ	DZRR (%)
0.5	2.08 (0.83, 1.87)	1.74 (1.06, 3.35)	0.00%	1.40 (0.85, 1.95)	1.38 (0.89, 1.72)	0.60%	**1.26 (0.83, 1.87)**	**1.29 (0.97, 1.8)**	18.12%
1.0	5.16 (2.29, 7.95)	2.78 (1.46, 6.96)	0.00%	1.46 (1.09, 1.80)	1.46 (1.08, 2.19)	**46.37%**	**1.37 (0.93, 2.01)**	**1.39 (1.03, 1.99)**	**47.03%**
1.5	10.95 (6.3, 13.29)	4.7 (2.70, 7.89)	0.00%	1.67 (1.25, 2.23)	1.78 (1.32, 2.55)	**59.63%**	**1.63 (1.14, 2.40)**	**1.60 (1.10, 2.26)**	**56.39%**

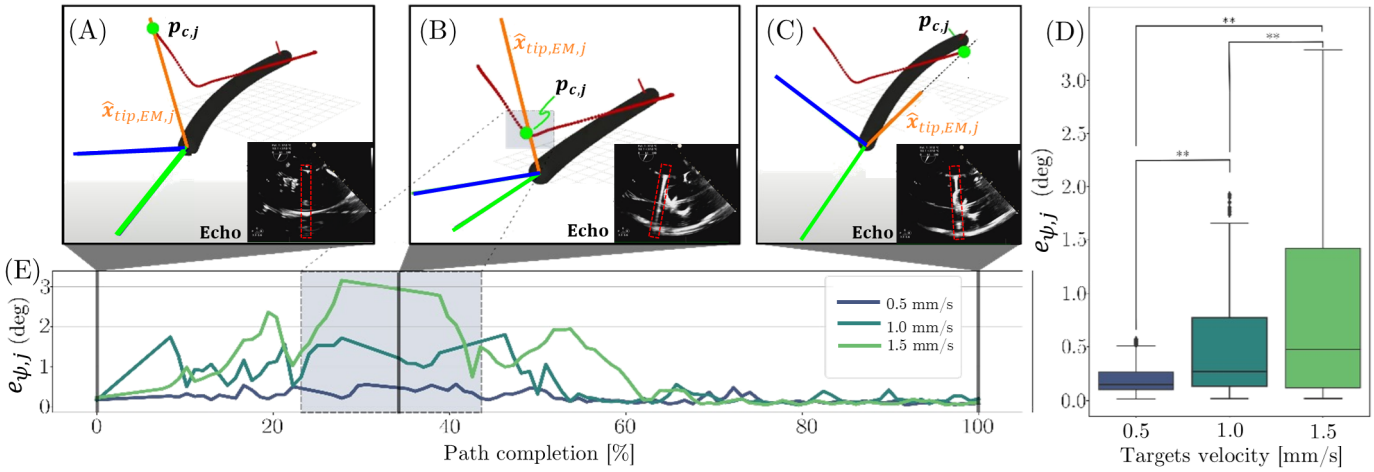

Fig. 9. Results of the catheter following experiment. (A–C) Snapshots from three key stages of the procedure, including the initial phase, shraddling phase, and final phase. The reconstructed 3D model of the TEE probe (black) is shown tracking the catheter tip (green point). Corresponding echo images are provided, with the catheter highlighted by a red box. (D) Distribution of angular errors at three different catheter velocities: 0.5 mm/s, 1.0 mm/s, and 1.5 mm/s ($**$: p-value < 0.005). (E) Angular error plotted along the catheter trajectory, where significant deviations are highlighted in blue.

guidelines [5], [34], the operator first advanced the catheter, ensuring proper positioning for subsequent maneuvers. After successful insertion, mediolateral bending maneuvers were performed to adjust the catheter's orientation. The EM tracking system continuously recorded the catheter's position, providing a reference catheter path for evaluating the TEE robot's catheter-following performance.

The recorded path of the catheter was discretized into 100 points and used as the path for the catheter following algorithm, representing the desired target positions ($\boldsymbol{p}_{c,j}$). The experiment was conducted at three different velocities: slow (0.5 mm/s), medium (1.0 mm/s), and fast (1.5 mm/s) to assess speed limitations of the system. The Kruskal–Wallis test was employed to statistically analyze differences among the various test conditions.

As demonstrated in Supplementary Video 4, the ultrasound imaging plane was fixed at an angle of 61°, and the catheter remained continuously visible within the echo image while the TEE probe autonomously followed its motion. However, since the echo image is 2D, it cannot accurately capture or quantify orientation errors associated with the probe's pose. To address this limitation, the primary performance metric used in this evaluation was the angular error ($e_{\psi,j}$), which is the angle between the current positive x-axis of the TEE tip measured by the EM sensor ($\hat{\boldsymbol{x}}_{tip,EM,j}$) and the direction vector ($\boldsymbol{t}_j$) from the current TEE tip position ($\hat{\boldsymbol{p}}_{tip,j}$) to desired target position ($\boldsymbol{p}_{c,j}$), as follow:

$$e_{\psi,j} = \cos^{-1}\left(\frac{\boldsymbol{t}_j \cdot \hat{\boldsymbol{x}}_{tip,EM,j}}{||\boldsymbol{t}_j|| \cdot ||\hat{\boldsymbol{x}}_{tip,EM,j}||}\right) \tag{13}$$

As depicted in Fig. 9, a marked increase in angular errors is observed as the path progresses to approximately 40% completion. This corresponds to the transition point where the catheter movement shifts from advancement to mediolateral bending (Fig. 9B). Fig. 9D illustrates the error distributions observed during the experiments. At the lowest speed (0.5 mm/s), the maximum angular error is 0.6°, remaining below 1% of the total field of view (90°). Even at the highest frequency (1.5 mm/s) the maximum error increases to only 3.2°, remaining below 4% of the total field. These results highlight the robustness of the proposed controller, demonstrating its ability to maintain accuracy across varying operational speeds.

V. CONCLUSION

In this work, we propose a robotic TEE system with a collaborative control framework based on real-time feedback from EM sensors for autonomous TEE procedures. The framework incorporates a hybrid adaptive controller that combines a CC model for solving the robot's inverse kinematics with a PID controller to minimize position errors. By employing an offline hysteresis dataset, the hysteresis curves were identified through the bivariate spline optimization method. The PID control parameters dynamically adapt to the varying hysteresis stages of the tendon-driven mechanism during bending movements.

We validated the proposed method using a realistic cardiac phantom, demonstrating its applicability to assist the TMVr procedure by (1) continuously tracking the catheter during device deployment, maintaining consistent visibility in the echo image, and (2) automatically reproducing the same imaging pose for post-procedure evaluation, eliminating the need for manual probe repositioning. The proposed approach completely relieves the sonographer from the physical workload associated with manual probe handling and from the need to wear heavy radiation-protective garments, allowing them to operate remotely outside the operating room and thus be free from radiation exposure. Furthermore, since the proposed collaborative control algorithm is a position-based visual servoing method that does not rely on direct control of the ultrasound crystal or on the adjustment of imaging parameters at the echo console, it is inherently independent of the probe model and imaging system. This design enables seamless integration with different generations of TEE probes and ultrasound platforms.

To enhance robustness for clinical application, future work will focus on implementing intraoperative image-to-image registration between pre-operative CT data and intraoperative 3D echo images. This approach can compensate for physiological motion such as respiration and heartbeat, allowing continuous updates of the 3D anatomical model during the procedure. Moreover, predefined surgical paths or implant delivery targets can be mapped onto the echo images to provide real-time visual guidance for the interventionalist. Regarding registration of the EM tracking frame with the CT data, bony anatomical landmarks (e.g., vertebrae or ribs) may serve as stable fiducials for static point-to-point registration. Another critical aspect is improving the safety of probe–tissue interaction, where fiber Bragg grating (FBG) sensors can be integrated to measure contact forces and prevent tissue damage [35]. Nonetheless, the results and workflow demonstrated in this work show that the proposed robotic TEE system and collaborative control framework have significant potential to assist interventionists in catheter navigation.

REFERENCES

[1] B. Bozkurt, A. J. Coats, H. Tsutsui, M. Abdelhamid, S. Adamopoulos, N. Albert, S. D. Anker, J. Atherton, M. Böhm, J. Butler *et al.*, "Universal definition and classification of heart failure: a report of the heart failure society of america, heart failure association of the european society of cardiology, japanese heart failure society and writing committee of the universal definition of heart failure," *Journal of cardiac failure*, vol. 27, no. 4, pp. 387–413, 2021.

[2] R. Ro, D. Bamira, S. Bernard, A. Vainrib, H. Ibrahim, C. Staniloae, M. R. Williams, and M. Saric, "Transesophageal echocardiographic screening for structural heart interventions," *Current Cardiology Reports*, vol. 25, no. 3, pp. 97–107, 2023.

[3] F. A. Flachskampf, P. F. Wouters, T. Edvardsen, A. Evangelista, G. Habib, P. Hoffman, R. Hoffmann, P. Lancellotti, M. Pepi, E. A. of Cardiovascular Imaging Document reviewers: Erwan Donal, and F. Rigo, "Recommendations for transoesophageal echocardiography: Eacvi update 2014," *European Heart Journal–Cardiovascular Imaging*, vol. 15, no. 4, pp. 353–365, 2014.

[4] M. D. Puchalski, G. K. Lui, W. C. Miller-Hance, M. M. Brook, L. T. Young, A. Bhat, D. A. Roberson, L. Mercer-Rosa, O. I. Miller, D. A. Parra *et al.*, "Guidelines for performing a comprehensive transesophageal echocardiographic: examination in children and all patients with congenital heart disease: recommendations from the american society of echocardiography," *Journal of the American Society of Echocardiography*, vol. 32, no. 2, pp. 173–215, 2019.

[5] J. Hausleiter, T. J. Stocker, M. Adamo, N. Karam, M. J. Swaans, and F. Praz, "Mitral valve transcatheter edge-to-edge repair," *EuroIntervention*, vol. 18, no. 12, p. 957, 2023.

[6] A. B. Freitas-Ferraz, M. Bernier, R. Vaillancourt, P. A. Ugalde, F. Nicodème, J.-M. Paradis, J. Champagne, G. O'Hara, L. Junquera, D. Del Val *et al.*, "Safety of transesophageal echocardiography to guide structural cardiac interventions," *Journal of the American College of Cardiology*, vol. 75, no. 25, pp. 3164–3173, 2020.

[7] A. Jain, L. Gutierrez, and D. Stanton, "3d tee registration with x-ray fluoroscopy for interventional cardiac applications," in *Functional Imaging and Modeling of the Heart: 5th International Conference, FIMH 2009, Nice, France, June 3-5, 2009. Proceedings 5*, pp. 321–329. Springer, 2009.

[8] X. Zhang, I. Tamadon, B. I. F. Jara, V. Cannizzaro, A. Peloso, A. Bicchi, A. Aliverti, E. Votta, A. Menciassi, and E. De Momi, "Design and hysteresis compensation of a telerobotic system for transesophageal echocardiography," *IEEE Robotics and Automation Letters*, 2024.

[9] Z. Yang, L. Yang, M. Zhang, C. Zhang, S. C. H. Yu, and L. Zhang, "Ultrasound-guided catheterization using a driller-tipped guidewire with combined magnetic navigation and drilling motion," *IEEE/ASME transactions on mechatronics*, vol. 27, no. 5, pp. 2829–2840, 2021.

[10] Z. Jiang, S. E. Salcudean, and N. Navab, "Robotic ultrasound imaging: State-of-the-art and future perspectives," *Medical image analysis*, p. 102878, 2023.

[11] E. Zakeri, A. Spilkin, H. Elmekki, A. Zanuttini, L. Kadem, J. Bentahar, W.-F. Xie, and P. Pibarot, "Robust deep feature ultrasound image-based visual servoing: Focus on cardiac examination," *IEEE/ASME Transactions on Mechatronics*, 2025.

[12] S. Wang, D. Singh, D. Johnson, K. Althoefer, K. Rhode, and R. J. Housden, "Robotic ultrasound: View planning, tracking, and automatic acquisition of transesophageal echocardiography," *IEEE Robotics & Automation Magazine*, vol. 23, no. 4, pp. 118–127, 2016.

[13] Y. Xie, J. Guo, Z. Deng, X. Hou, J. Housden, K. Rhode, H. Liu, Z.-G. Hou, and S. Wang, "Robot-assisted trans-esophageal ultrasound and the virtual admittance-based master-slave control method thereof," *IEEE/ASME Transactions on Mechatronics*, vol. 28, no. 5, pp. 2505–2516, 2023.

[14] R. Kreher, T. Groscheck, K. Qarri, B. Preim, A. Schmeisser, T. Rauwolf, R. C. Braun-Dullaeus, and S. Engelhardt, "A novel calibration phantom for combining echocardiography with electromagnetic tracking," in *Current Directions in Biomedical Engineering*, vol. 6, no. 1, p. 20200003. De Gruyter, 2020.

[15] X. Zhang, A. Sridhar, X. T. Ha, S. Z. Mehdi, A. Fortuna, M. Magro, A. Peloso, A. Bicchi, M. Ourak, A. Aliverti *et al.*, "Path tracking control of a steerable catheter in transcatheter cardiology interventions," *International Journal of Computer Assisted Radiology and Surgery*, vol. 19, no. 4, pp. 757–766, 2024.

[16] W. Wang, Z. Xu, A. M. Zeidan, C. Saija, Y. Zheng, M. Arena, S. Wang, R. J. Housden, and K. Rhode, "Compact design and image-space pose control of a robot for tendon-driven concentric catheters in mitral repair interventions," *IEEE/ASME Transactions on Mechatronics*, 2025.

[17] R. S. Penning, J. Jung, N. J. Ferrier, and M. R. Zinn, "An evaluation of closed-loop control options for continuum manipulators," in *2012 IEEE International Conference on Robotics and Automation*, pp. 5392–5397. IEEE, 2012.

[18] B. Bardou, P. Zanne, F. Nageotte, and M. de Mathelin, "Control of a multiple sections flexible endoscopic system," in *2010 IEEE/RSJ International Conference on Intelligent Robots and Systems*, pp. 2345–2350. IEEE, 2010.

[19] A. Degirmenci, P. M. Loschak, C. M. Tschabrunn, E. Anter, and R. D. Howe, "Compensation for unconstrained catheter shaft motion in cardiac catheters," in *2016 IEEE International Conference on Robotics and Automation (ICRA)*, pp. 4436–4442. IEEE, 2016.

[20] A. A. Alqumsan, S. Khoo, and M. Norton, "Robust control of continuum robots using cosserat rod theory," *Mechanism and Machine Theory*, vol. 131, pp. 48–61, 2019.

[21] P. Tucan, O.-M. Vanta, C. Vaida, M. Ciupe, D. Sebeni, A. Pisla, S. Stiole, D. Lupu, Z. Major, B. Gherman *et al.*, "Fuzzy adaptive control for a 4-dof hand rehabilitation robot," in *Actuators*, vol. 14, no. 7, p. 351. MDPI, 2025.

[22] Q. Chen, W. Li, and G. Chen, "Fuzzy p+ id controller for a constant tension winch in a cable laying system," *IEEE Transactions on Industrial Electronics*, vol. 64, no. 4, pp. 2924–2932, 2016.

[23] W. Ba, X. Dong, A. Mohammad, M. Wang, D. Axinte, and A. Norton, "Design and validation of a novel fuzzy-logic-based static feedback controller for tendon-driven continuum robots," *IEEE/ASME Transactions on Mechatronics*, vol. 26, no. 6, pp. 3010–3021, 2021.

[24] O. Mohareri, J. Ischia, P. C. Black, C. Schneider, J. Lobo, L. Goldenberg, and S. E. Salcudean, "Intraoperative registered transrectal ultrasound guidance for robot-assisted laparoscopic radical prostatectomy," *The Journal of urology*, vol. 193, no. 1, pp. 302–312, 2015.

[25] P. M. Loschak, L. J. Brattain, and R. D. Howe, "Algorithms for automatically pointing ultrasound imaging catheters," *IEEE Transactions on Robotics*, vol. 33, no. 1, pp. 81–91, 2016.

[26] X. Zhang, M. C. Palumbo, F. Perico, M. Magro, A. Fortuna, T. Magni, E. Votta, A. Segato, and E. De Momi, "Robotic actuation and control of a catheter for structural intervention cardiology," in *2022 IEEE/RSJ International Conference on Intelligent Robots and Systems (IROS)*, pp. 5907–5913. IEEE, 2022.

[27] K. Tystad Lund, G. A. Tangen, and F. Manstad-Hulaas, "Electromagnetic navigation versus fluoroscopy in aortic endovascular procedures: a phantom study," *International journal of computer assisted radiology and surgery*, vol. 12, pp. 51–57, 2017.

[28] A. M. Franz, T. Haidegger, W. Birkfellner, K. Cleary, T. M. Peters, and L. Maier-Hein, "Electromagnetic tracking in medicine—a review of technology, validation, and applications," *IEEE transactions on medical imaging*, vol. 33, no. 8, pp. 1702–1725, 2014.

[29] G. Faoro, I. Tamadon, S. Tognarelli, and A. Menciassi, "A multi-sensorization approach to improve safety in transesophageal echocardiography," *IEEE Transactions on Medical Robotics and Bionics*, 2024.

[30] G. Beliakov, "Least squares splines with free knots: global optimization approach," *Applied mathematics and computation*, vol. 149, no. 3, pp. 783–798, 2004.

[31] F. Xia, J. Mao, J. Ding, and H. Yang, "Observation of normal appearance and wall thickness of esophagus on ct images," *European journal of radiology*, vol. 72, no. 3, pp. 406–411, 2009.

[32] V. I. Egorov, I. V. Schastlivtsev, E. V. Prut, A. O. Baranov, and R. A. Turusov, "Mechanical properties of the human gastrointestinal tract," *Journal of biomechanics*, vol. 35, no. 10, pp. 1417–1425, 2002.

[33] A. Parvaresh and S. A. A. Moosavian, "Modeling and model-free fuzzy control of a continuum robotic arm," in *2018 6th RSI International Conference on Robotics and Mechatronics (IcRoM)*, pp. 501–506. IEEE, 2018.

[34] G. Russo, A. d'Aiello, D. Pedicino, S. Kuwata, G. M. Sangiorgi, M. Taramasso, and F. Maisano, "Understanding transcatheter edge-to-edge repair "knobology": Advanced catheter steering for different scenarios of transseptal puncture," *Catheterization and Cardiovascular Interventions*, vol. 103, no. 7, pp. 1138–1144, 2024.

[35] T. O. Akinyemi, O. M. Omisore, W. Duan, G. Lu, Y. Al-Handerish, S. Han, and L. Wang, "Fiber bragg grating-based force sensing in robot-assisted cardiac interventions: A review," *IEEE Sensors Journal*, vol. 21, no. 9, pp. 10 317–10 331, 2021.

Xiu Zhang Xiu Zhang received the M.Sc. degree in Mechanical Engineering from Politecnico di Torino and the Ph.D. degree in Bioengineering from Politecnico di Milano. From 2025, He starts as a postdoctoral researcher in the Surgical Robotics and Allied Technologies Area at the BioRobotics Institute, Scuola Superiore Sant'Anna, Italy. His research focuses on robotic systems for image-guided cardiovascular interventions, with particular interests in autonomous control, reinforcement learning-based planning.

Benjamín Fortuño Benjamín Fortuño received his MSc in Biomedical Engineering from Politecnico di Milano, where he is currently pursuing a PhD. His research lies at the intersection of surgical robotics and autonomous control for surgical tasks. He has expertise in robot kinematics, learning-based control, and optimization methods. His main interest is enabling autonomy and precision in robot-assisted procedures through advanced AI and real-time control.

Matteo Di Mauro Matteo Di Mauro received the M.S. degree in Biomedical Engineering from Politecnico di Milano in 2024. He is currently pursuing the Ph.D in Artificial Intelligence in Biomedical Engineering, focusing on early detection and prevention of cardiac arrest using neural networks and deep learning techniques.

Vanessa Cannizzaro She received both her B.Sc. and M.Sc. degrees in Biomedical Engineering from Politecnico di Milano. Before starting her Ph.D., she conducted research on continuum robots for cardiovascular surgery. She is currently pursuing a Ph.D. at NEARLab MRS, Politecnico di Milano, in collaboration with the European Institute of Oncology (IEO), with a research focus on imaging guidance for thermal ablation procedures.

Angela Peloso Angela Peloso obtained MSc in Biomedical Engineering in 2021 at University of Padova. From 2021 to 2022 she was a research fellow at the University of Verona. She is currently enrolled as PhD Candidate at Politecnico di Milano. Her research has focused on path planning for autonomous steerable catheters under ARTERY project, and motion planning for continuum robotics

Anna Bicchi Anna Bicchi obtained MSc in Automation and Control Engineering from, in 2021. From 2021 to 2022, she was a research fellow and currently is a PhD candidate at Politecnico di Milano, her research focuses on modeling and control of continuum robot for minimally invasive surgery.

Luca Vicenti Luca Vicenti is a Biomedical Engineer with a Master's from TU Eindhoven and extensive experience in cardiovascular R&D and device simulation. Currently COO at Simulands AG, leading operations and innovation in advanced medical simulation technologies. Over a decade of experience in project management, therapy development, and clinical/preclinical support across Europe.

Andrea Aliverti Andrea Aliverti received the M.Sc. degree in electronics engineering and the Ph.D. degree in bioengineering from Politecnico di Milano, in 1992 and 1997, respectively. He is currently a Full Professor with the Department of Electronics, Information and Bioengineering (DEIB), Politecnico di Milano. His research interest biomedical instrumentation and sensors, wearable technology, biomedical imaging, AI applications in physiological data, signal and images.

Emiliano Votta Emiliano Votta received his PhD in bioengineering in 2006 from Politecnico di Milano, where he is currently an associate professor at the Department of Electronics, Information, and Bioengineering. He is an expert in cardiovascular biomechanics and computer modeling, with an emphasis on numerical simulations, mixed reality, and image analysis.

Arianna Menciassi Arianna Menciassi is a Full Professor of Biomedical Engineering at Scuola Superiore Sant'Anna (Pisa, Italy). She leads the Surgical Robotics and Allied Technologies Area. Her research focuses on the study and development of surgical and therapeutic robotic tools, procedures guided by ultrasound and magnetic fields, microrobotic interventions, and robotic artificial organs.

Elena De Momi Elena received her MSc in Biomedical Engineering in 2002, PhD in Bioengineering in 2006, and she is currently Full Professor in the Electronic Information and Bioengineering Department (DEIB) of Politecnico di Milano. She is co-founder of the Neuroengineering and Medical Robotics Laboratory, in 2008, being responsible of the Medical Robotics section.